OPTICS

Broadband uniform-efficiency OAM-mode detector

Suman Karan[1]*, Martin P. Van Exter[2], Anand K. Jha[1]*

The high-dimensional basis of orbital angular momentum (OAM) has several added and unique advantages for photonic quantum technologies compared to the polarization basis, which is only two-dimensional. However, one of the major roadblocks in implementing OAM-based applications with their full potentials is the absence of an ideal OAM-mode detector. Despite the plethora of efforts in the last three decades, currently, there is no OAM detector that can detect a broad OAM-mode spectrum, has uniform detection-efficiency over all the modes, measures the true spectrum, and works for an arbitrary quantum state without the need for any previous information. Here, we experimentally demonstrate just such an OAM detector. We report detection of pure and mixed OAM states with fidelities more than 98% and with measurement times of only a few minutes for dimensionalities up to 100. We expect our work to substantially boost the OAM-based photonic quantum technology efforts.

INTRODUCTION

In 1992, Allen *et al.* showed that a photon in a Laguerre-Gaussian (LG) mode, represented as $LG_p^{|l|}(\rho)e^{il\phi}$ in the transverse polar coordinates, carries $l\hbar$ orbital angular momentum (OAM). Here, l is an integer ranging from $-\infty$ to ∞ and is referred to as the OAM-mode index, whereas p is called the radial-mode index, ranges from 0 to ∞, and decides the radial profile of the mode (*1*). As the OAM of a photon provides a basis that is not only high-dimensional but also discrete, several OAM-based applications have been proposed and demonstrated, highlighting the added and unique advantages of the high-dimensional OAM basis for photonic quantum technologies compared to the two-dimensional polarization basis (*2*, *3*). These include demonstrating terabit-scale data transmission using OAM-mode multiplexing for long-distance communication through free space (*4*, *5*) and fiber (*6*), enhanced security and error tolerance for quantum communication protocols (*7*, *8*), efficient gate implementation (*9*, *10*), super-sensitive measurement in quantum metrology (*11*, *12*), and fundamental tests of quantum mechanics (*13*–*16*). The OAM basis has been shown to be the preferred basis for ground-to-ground and ground-to-satellite long-distance communications (*17*–*19*). More recently, the OAM basis has been used for demonstrating quantum cryptography within a city (*20*) and through outdoor underwater channel (*21*). High-dimensional quantum gates (*22*) and entanglement distribution (*23*) have been demonstrated with OAM modes. As an important advancement for long-distance communication, optical fibers have been demonstrated, which can carry several OAM modes up to a kilometer without substantial loss or cross-talk (*24*).

Although the push for exploiting OAM basis for quantum information technologies has been steadily increasing in the past three decades, one of the major roadblocks for implementing OAM-based applications with their full potential is the absence of an OAM detector that detects a broad range of modes with uniform detection efficiency, measures the true spectrum, and works for an arbitrary quantum state without the need for any previous information about the state. Consequently, developing such a detector has been an active area of research (*12*, *25*–*32*). There are several approaches to detecting the OAM of photonic quantum states.

One main approach (*25*, *26*), which is currently the most widely used, is based on displaying holograms specific to different OAM modes onto a spatial light modulator (SLM) and then measuring the intensity of the $(l = 0, p = 0)$ mode at the first diffraction order of the SLM using a single-mode fiber (SMF). This way, by placing holograms specific to different input OAM modes in a sequential manner, one is able to measure the spectrum. However, an SMF has nonuniform coupling efficiencies for different OAM modes (*33*) and therefore the efficiency of this method decreases with increasing l, making it unsuitable for broadband detection. Furthermore, an SMF detects primarily the $p = 0$ mode and therefore this method does not work for quantum states in which the OAM is distributed over multiple radial modes (*34*, *35*). Even the $p = 0$ mode detection can be efficient only if one has the previous knowledge of the generation beam waist (see section S1 for a detailed analysis). The SMF-based OAM detection method has also been integrated with compressive sensing techniques for faster measurement of up to 17-dimensional nearly pure states in the OAM basis (*36*). However, besides the fact that this method works only for nearly pure states and requires previous knowledge of the state to achieve faster detection, it suffers from all the limitations faced by the SMF-based schemes. More recently, the traditional SMF-based techniques for measuring just the $p = 0$ modes, which works on the principle of phase flattening, have been extended to also detect $p \neq 0$ radial modes by implementing a smart technique referred to as the intensity flattening (*37*). With this, detection of up to 8 radial modes as well as the first 55 lowest-order LG modes have been demonstrated. However, this detector suffers from considerable loss and requires previous information about the mode space and its dimensionality to optimize the detection efficiency of different modes. Even more recently, advanced techniques for measuring spatial modes have been demonstrated using multiple SLMs and an SMF (*38*–*40*). These methods provide more control as far as optimizing the mode-dependent efficiency is concerned. Nonetheless, due to the inherent reflections at multiple SLMs, the loss in general is high, and for the better optimization of detection efficiency, one need to have previous information about the input state.

The second set of approaches, which do not use an SMF and thus do not suffer from the coupling-efficiency issues, rely on reconstructing the OAM spectrum by measuring the angular coherence function (*12*, *27*–*29*). An effective way to measure the angular coherence function is by measuring the visibility in a Mach-Zehnder

[1]Department of Physics, Indian Institute of Technology Kanpur, Kanpur, UP 208016, India. [2]Huygens-Kamerlingh Onnes Laboratory, Leiden University, P.O. Box 9504, 2300 RA Leiden, Netherlands.
*Corresponding author. Email: karans@iitk.ac.in (S.K.); akjha@iitk.ac.in (A.K.J.)

interferometer of the interference between two optical fields that are rotated with respect to each other (*27*, *28*). The experimental implementation of such OAM detectors has been carried out for diagonal mixed states at high-light levels (*27*) as well as for entangled two-photon states (*28*), in which case the method even becomes phase insensitive. However, we note that the scheme in (*28*) works only for measuring the OAM Schmidt spectrum of entangled photons but does not work for single-photon OAM states. Another way of measuring the angular coherence function (*12*, *29*) is by using angular double slits (*41*); however, since only a very small portion of the incident field can be used for detection, this method is not suitable at single-photon levels. The other approaches to measuring the OAM spectrum include techniques based on rotational Doppler frequency shift (*30*, *31*) and concatenated Mach-Zehnder interferometers (*32*). However, due to experimental challenges, these approaches (*30*–*32*) have been demonstrated only for quantum states consisting of just a few OAM modes.

More recently, there have been several works that have also overcome some of the limitations mentioned above. For example, detection of 27-dimensional pure states has been demonstrated using weak measurement techniques (*42*). Such weak measurement-based technique can work for measuring a general density matrix as well, as proposed theoretically (*43*) and demonstrated experimentally (*44*) in the position basis. However, there has been no experimental demonstration of weak measurement-based technique for measuring an arbitrary quantum state in the OAM basis. Next, using interferometric schemes, detection of up to 25-dimensional pure states (*45*) and more than 200-dimensional mixed diagonal states (*35*, *46*) has been demonstrated. However, these schemes have so far been demonstrated only for specific classes of quantum states and not for an arbitrary quantum state in the OAM basis. Another technique that overcomes several of the limitations mentioned above is based on the idea of measuring the azimuthal Wigner distribution function and thereby reconstructing the state in the OAM basis (*47*). Although this technique in principle works for arbitrary high-dimensional states, it has so far been demonstrated only up to 7-dimensional states with fidelity up to only 90%.

A slightly different set of efforts has been through making an OAM sorter, which aims to spatially separate OAM modes based on their mode index l (*42*, *48*–*52*). An ideal OAM sorter works as a perfect OAM detector. However, the current OAM sorter implementations involve either multiple diffractive elements and thus suffer from losses that are very difficult to estimate (*42*, *48*–*50*), or sort the OAM modes with substantial overlap between neighboring modes (*52*), or need spatially separated modes at the input itself (*51*). Therefore, these cannot be used as OAM detectors. In contrast, here, we experimentally demonstrate an OAM-mode detector that works for a broad range of modes, has uniform detection efficiency over the entire range, measures the true mode spectrum, and works for an arbitrary quantum state without the need for any previous information.

RESULTS

Theory of OAM spectrum detection

We consider an arbitrary $2N + 1$-dimensional single-photon quantum state in the OAM basis given by the density matrix

$$\rho_{\text{in}} = \sum_{l_1,l_2=-N}^{+N} \sum_{p_1,p_2=0}^{\infty} C_{l_1,l_2}^{p_1,p_2} \, |l_1, p_1\rangle \langle l_2, p_2| \tag{1}$$

Here, $|l_1, p_1\rangle$ is a single-photon state with mode indices (l_1, p_1) and $C_{l_1,l_2}^{p_1,p_2}$ is the density matrix element corresponding to indices (l_1, p_1) and (l_2, p_2). The projection of $|l_1, p_1\rangle$ on the transverse polar basis state $|\rho, \phi\rangle$ is given by $\langle \rho, \phi \,|\, l, p\rangle = \text{LG}_p^{|l|}(\rho) e^{-il\phi}$. Figure 1C shows the schematic of our experimental setup. The state ρ_{in} enters the interferometer having an image rotator (IR) oriented at angle θ in one of the two arms

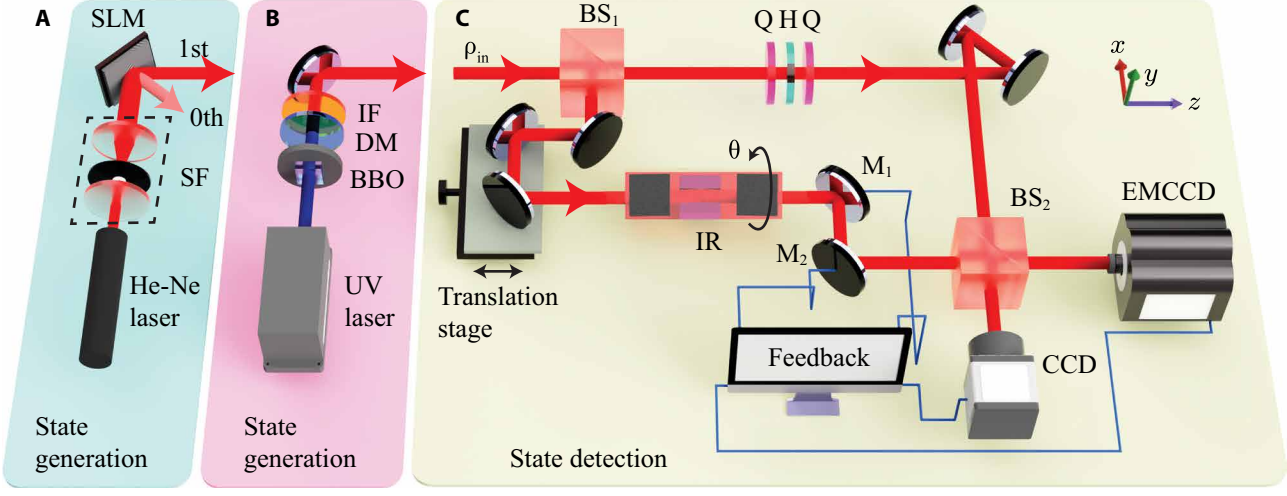

Fig. 1. Experimental setup. (**A**) Schematic of the experimental setup for generating single-photon quantum states using an attenuated He-Ne laser and an SLM. (**B**) Schematic of the experimental setup for generating single-photon quantum states through SPDC. (**C**) Schematic of the experimental setup of the proposed OAM detector. Q and H stand for quarter- and half-wave plates. The combination Q-H-Q is geometric phase unit comprising a quarter-wave plate (Q) at 45°, a half-wave plate (H) at δ / 2, and another quarter-wave plate at 45°, resulting in a geometric phase of δ. The angular deviation of the beam caused by IR is adjusted by two electronically controlled mirrors M_1 and M_2 using an automatic feedback mechanism. In the above figure, DM is the dichroic mirror to block the UV pump; IF is the interference filter of central wavelength 810 nm with bandwidth of 10 nm; BS stands for a beam splitter; IR is a homebuilt image rotator; and SF is a spatial filter.

and gets detected using a single-photon sensitive electron-multiplied charge-coupled device (EMCCD) camera. IR is a homebuilt wavefront rotating device consisting of three mirrors. As depicted in the figure, we consider the beam propagation direction to be along $\hat{\mathbf{z}}$ and the azimuthal angle $\phi = 0$ to be along $\hat{\mathbf{x}}$. We define the $\theta = 0$ rotation angle to be when the three mirrors are on the *x*-*z* plane. The transformation of the field due to a mirror reflection can be written as $\phi \rightarrow \pi - \phi$, while that due to the IR can be written as $\phi \rightarrow -\phi + \pi + 2\theta$. Therefore, we express the projection operators for the mirror and the IR as $\hat{M} = \sum_{l,p} e^{-il\pi} |-l,p\rangle\langle l,p|$ and $\hat{\mathrm{IR}}(\theta) = \sum_{l,p} e^{-il(\pi+2\theta)} |-l,p\rangle\langle l,p|$, respectively (see sections S2 and S3 for the detailed derivations). For an $\hat{\mathbf{x}}$-polarized input, the polarization state of the field after passing through the IR is given by $\hat{\epsilon}(\theta) = \cos[\psi(\theta)]\hat{\mathbf{x}} + \sin[\psi(\theta)] e^{i\chi(\theta)}\hat{\mathbf{y}}$ (*53*). Therefore, the projection operator at the EMCCD plane becomes $\hat{P} = \sum_{l=-\infty}^{\infty} \sum_{p=0}^{\infty} e^{i(-l\pi+\beta_1-\omega_0 t_1+\gamma_1)} [|k_1|\hat{\mathbf{x}} + |k_2| e^{-i(\delta+2l\theta)} \hat{\epsilon}(\theta)] |-l,p\rangle\langle l,p|$, where ω_0 is the central frequency and $k_1 = |k_1| e^{i\gamma_1}$ and $k_2 = |k_2| e^{i\gamma_2}$ are the fractions of the input field passing through the two arms; these fractions depend on the reflection and the transmission coefficients of the beam splitters and the mirrors; $\delta = (\beta_1 - \beta_2) - \omega_0(t_1 - t_2) + \gamma_1 - \gamma_2$, where t_1 and t_2 are the photon travel times, and β_1 and β_2 are the nondynamical phases in the two arms. The combination Q-H-Q is used for introducing a geometric phase δ. The density matrix at the EMCCD plane is given by $\rho_{\mathrm{out}} = \hat{P}\rho_{\mathrm{in}}\hat{P}^{\dagger}$, and thus, the total photon detection probability is given by $I_{\mathrm{out}}^{\delta}(\theta) = \int_0^{\infty} \int_0^{2\pi} \langle \rho, \phi | \rho_{\mathrm{out}} | \rho, \phi \rangle \, \rho d\rho \, d\phi$ (see section S4 for detailed derivation)

$$I_{\mathrm{out}}^{\delta}(\theta) = \sum_{l=-N}^{N} \sum_{p=0}^{\infty} C_{l,l}^{p,p} \left[|k_1|^2 + |k_2|^2 + 2|k_1||k_2| \cos[\psi(\theta)] \cos(\delta + 2l\theta) \right] \quad (2)$$

The OAM spectrum of the input state S_l is obtained by summing $C_{l,l}^{p,p}$ over all possible p modes, i.e., $S_l = \sum_{p=0}^{\infty} C_{l,l}^{p,p}$. We note that our detection scheme does not require measurements of spatially resolved photon detection probability and is therefore not limited by the spatial resolution of the EMCCD in contrast to several other schemes (*35*, *45*, *46*). In realistic experimental situations, the measured photon detection probability always contains some noise contributions $I_n^{\delta}(\theta)$, the sources of which in our experiments are the ambient light and the dark count of the EMCCD. Thus, the measured probability becomes $\bar{I}_{\mathrm{out}}^{\delta}(\theta) = I_n^{\delta}(\theta) + I_{\mathrm{out}}^{\delta}(\theta)$. To bypass such contributions, we use the two-shot technique (*35*) and perform the measurements at $\delta = \delta_c$ and $\delta = \delta_d$. We assume that the shot-to-shot noise remains constant and that the spectrum is symmetric, that is, $I_n^{\delta_c}(\theta) \approx I_n^{\delta_d}(\theta)$ and $S_l = S_{-l}$. The difference probability $\Delta\bar{I}_{\mathrm{out}}(\theta) = \bar{I}_{\mathrm{out}}^{\delta_c}(\theta) - \bar{I}_{\mathrm{out}}^{\delta_d}(\theta)$ can therefore be written as $\Delta\bar{I}_{\mathrm{out}}(\theta) = 2|k_1||k_2| \cos[\psi(\theta)] (\cos\delta_c - \cos\delta_d) \sum_{l=-N}^{+N} S_l \cos 2l\theta$. For bypassing the polarization effects manifesting as $\cos[\psi(\theta)]$, we work with the polarization-corrected difference probability $\Delta I_{\mathrm{out}}(\theta) = \Delta\bar{I}_{\mathrm{out}}(\theta) / \cos[\psi(\theta)]$

$$\Delta I_{\mathrm{out}}(\theta) = 2|k_1||k_2| \sum_{l=-N}^{N} S_l (\cos\delta_c - \cos\delta_d) \cos 2l\theta \quad (3)$$

Since $\cos[\psi(\theta)]$ is the $\hat{\mathbf{x}}$-projection of the field, we have

$$\cos[\psi(\theta)] = \sqrt{\frac{|\hat{\epsilon}(\theta)\cdot\hat{\mathbf{x}}|^2}{|\hat{\epsilon}(\theta)|^2}} = \sqrt{\frac{I_{2x}(\theta)}{I_2^{\mathrm{tot}}}} \quad (4)$$

where I_2^{tot} and $I_{2x}(\theta)$ are the total probability and the probability along $\hat{\mathbf{x}}$ of the field passing through the IR (see Materials and Methods for the experimental measurement of $\cos[\psi(\theta)]$). We define the measured OAM spectrum $\bar{S}_l$ to be

$$\bar{S}_l \equiv \int_0^{\pi} \Delta I_{\mathrm{out}}(\theta) \cos(2l\theta) d\theta = 2|k_1||k_2| (\cos\delta_c - \cos\delta_d) S_l \quad (5)$$

We note that $\bar{S}_l$ is not normalized but is proportional to the true OAM spectrum S_l. Therefore, using the fact that $\mathrm{Tr}(\rho_{\mathrm{in}}) = 1$, we obtain the true OAM spectrum as

$$S_l = \bar{S}_l \Big/ \left(\sum_{l=-N}^{+N} \bar{S}_l \right) \quad (6)$$

To estimate the measurement accuracy of our experimental scheme, we use the coefficient of determination R^2

$$R^2 \equiv \frac{\sum_{l=-N}^{+N} (S_l^{ob} - S_l^{in})^2}{\sum_{l=-N}^{+N} (S_l^{in} - \langle S_l^{in} \rangle)^2} \times 100\,\% \quad (7)$$

where S_l^{in} and S_l^{ob} are the input and the observed OAM spectra, and $\langle S_l^{\mathrm{in}} \rangle$ is the average of S_l^{in}.

Although in this section we have worked out the theory only for symmetric spectrum, in which case $S_l = S_{-l}$, our scheme works for nonsymmetric spectrum as well (see section S5). However, for a nonsymmetric spectrum, our scheme requires four intensity measurements instead of just two in the case of a symmetric spectrum. So, in situation in which one has the previous information that the spectrum is symmetric, one can measure the spectrum using only two intensity measurements. Otherwise, using four intensity measurements, one can measure any spectra, symmetric or asymmetric.

Experimental setup

We use two separate methods for generating a variety of single-photon quantum states in the OAM basis. Figure 1A is the schematic of the experimental setup for generating states using an attenuated He-Ne laser and an SLM, while Fig. 1B is that using the nonlinear optical process of spontaneous parametric down-conversion (SPDC). The generated states are detected using the proposed OAM detector, the schematic setup of which is shown in Fig. 1C. The setup involves an EMCCD camera for ensuring that the detection is at the single-photon level. We report experimental measurements for various different types of single-photon OAM states in Figs. 2 to 5. In each of these figures, panels (A) and (B) show the plots of $\bar{I}_{\mathrm{out}}^{\delta}(\theta)$ as a function of θ at $\delta = \delta_c \approx 0$ and $\delta_d \approx \pi$. Panel (C) presents the measured polarization-corrected difference probability $\Delta I_{\mathrm{out}}(\theta)$; the red dots are the experiments, and the solid green line is the theory. Using Eq. 6, we calculate S_l from the measured $\Delta I_{\mathrm{out}}(\theta)$ and plot them in panel (D), where the blue bars are for the observed

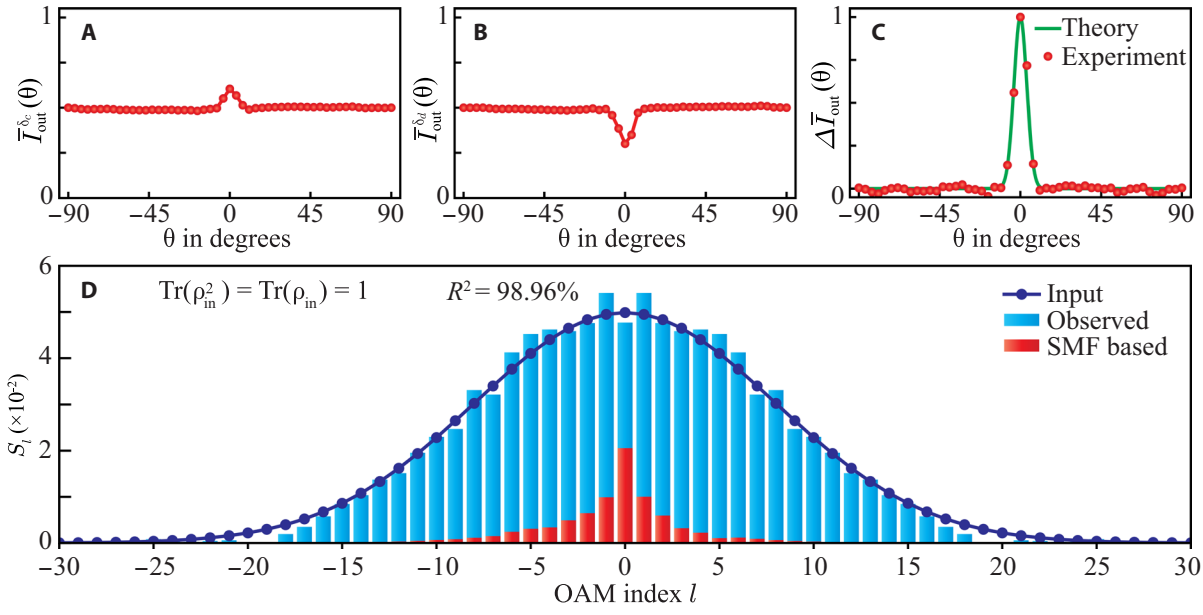

Fig. 2. Experimentally measured OAM spectrum for a 50-dimensional pure state $\mathbf{Tr}(\rho_{in}^2) = \mathbf{Tr}(\rho_{in}) = 1$. (**A** and **B**) Plots of the photon detection probability $\bar{I}_{out}^{\delta}(\theta)$ as a function of the rotation angle θ at $\delta = \delta_c \approx 0$ and $\delta = \delta_d \approx \pi$. (**C**) Experimentally measured polarization-corrected difference probability $\Delta I_{out}(\theta)$ as a function of θ. The red dots are the experiments, and the solid green line is the theory. (**D**) Reconstructed OAM spectrum. Blue bars are the measured spectrum, while the blue dots are the input spectrum; the red bars represent the performance of an SMF-based detector.

and the blue dots are for the input states. The red bars represent the performance of the SMF-based method (*25*, *26*) in the same situation with an SLM that has 50% diffraction efficiency in the first order. The measurement accuracy R^2 is shown inside each panel (D) (see Materials and Methods for details on experimental techniques, procedures, analysis, etc.).

Generating quantum states using an attenuated He-Ne laser and an SLM

For generating OAM states using the experimental setup of Fig. 1A, we use a Newport He-Ne laser of wavelength 633 nm followed by an SLM. Using the method by Arrizón *et al.* (*54*), we generate various input states ρ_{in}. First, we generate a pure quantum state with its OAM spectrum in the form of a Gaussian function of SD equal to 8. Figure 2 presents the experimental results. We obtain the measurement accuracy R^2 of 98.96%. Next, we generate a general mixed state by incoherently adding two pure states in 0.54 and 0.46 proportion (*55*); the pure states have Gaussian OAM spectra with SDs equal to 10 and 6. For details on how a general mixed state is produced using an SLM, see (*56*). Figure 3 shows the experimental results, with $R^2 = 98.58\%$. Finally, we demonstrate that our OAM detector is capable of detecting not only a continuous set of OAM modes but also a discrete set. For this purpose, we generate a state with five OAM modes ($l = 0, \pm 4, \pm 8$) with equal weightage and present the experimental results in Fig. 4, with $R^2 = 98.27\%$.

Generating quantum states using SPDC

Although one can synthesize an arbitrary single-photon quantum states using an attenuated He-Ne laser and an SLM, the implementation always introduces some generation errors. Such errors can be avoided if a quantum state is generated through some natural process. SPDC, a second-order nonlinear effect, is one such process, which naturally generates single-photon quantum states in the form of diagonal mixed state. So, for generating diagonal mixed states, we use SPDC, in which a pump photon gets down-converted into two separate photons called the signal and idler (*57*), and for a Gaussian pump field, the states of both the signal and idler photons are diagonal mixed states in the OAM basis (*12*, *28*). The spectrum S_l of each of the two photons depends on several experimental parameters such as the pump beam waist w_0, crystal thickness L, and phase-matching angle θ_p (*49*, *57*). Using SPDC in a β-barium borate (BBO) crystal with collinear phase-matching condition, we experimentally generate single-photon diagonal mixed states using the setup depicted in Fig. 1B, with $\theta_p = 28.668°$, $L = 15$ mm, and $w_0 = 388$ μm. Figure 5 presents the experimental results, with $R^2 = 99.85\%$. We find that for the same state, the detection efficiency of the SMF-based measurement scheme is relatively much less, is mode dependent, and becomes negligible for OAM modes with $|l| > 20$.

Note on the generation error

We note that the measurement accuracy of the results reported in Figs. 2D, 3D, and 4D is smaller than that of Fig. 5D. We attribute this to the error in the generation process adopted to produce the states. For the results reported in Figs. 2D, 3D, and 4D, the state was generated using an SLM. The input spectrum plotted as blue dots in Figs. 2D to 4D is what we ideally desired to generate, but it is not what was generated by the SLM due to all the associated generation errors. Nonetheless, we plotted the blue dots as input spectrum. Therefore, the inaccuracies in Figs. 2D to 4D are primarily because of the error in the generation process and thus in the plotted input spectrum but not because of the error in the observed spectrum. However, we note that, if the state generation has no error, the match between the input

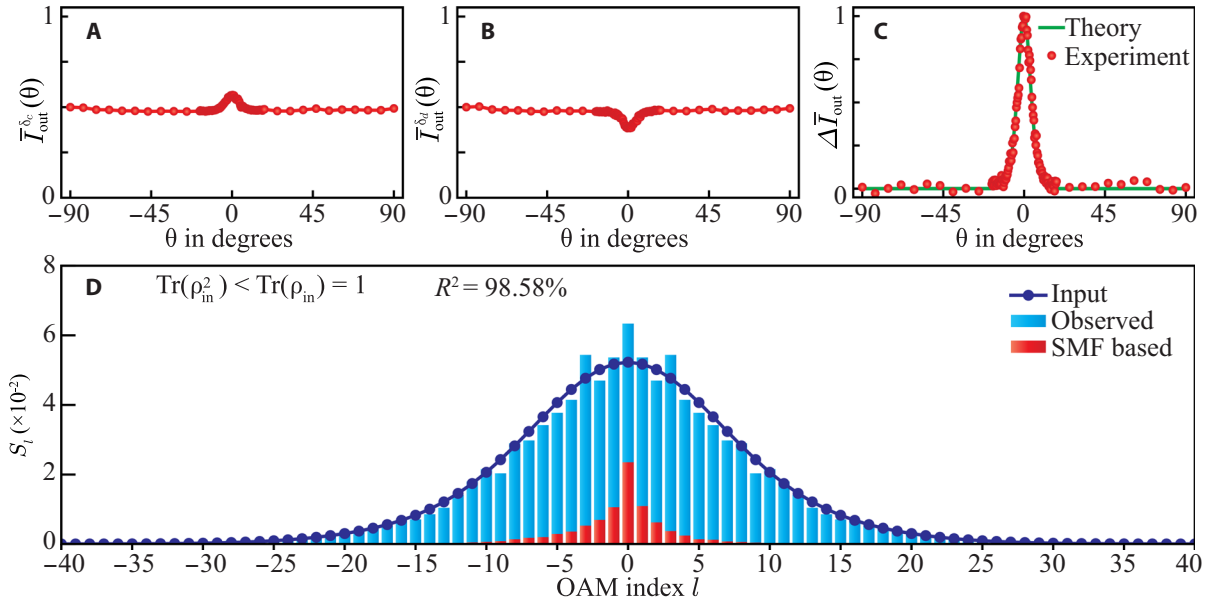

Fig. 3. Experimentally measured OAM probability distribution for a 80-dimensional general mixed state $\mathbf{Tr}(\rho_{in}^2) < \mathbf{Tr}(\rho_{in}) = 1$. (**A** and **B**) Plots of the photon detection probability $\bar{I}^{\delta}_{out}(\theta)$ as a function of the rotation angle θ at $\delta = \delta_c \approx 0$ and $\delta = \delta_d \approx \pi$. (**C**) Experimentally measured polarization-corrected difference probability $\Delta I_{out}(\theta)$ as a function of θ. The red dots are the experiments, and the solid green line is the theory. (**D**) Reconstructed OAM spectrum. Blue bars are the measured spectrum, while the blue dots are the input spectrum; the red bars represent the performance of an SMF-based detector.

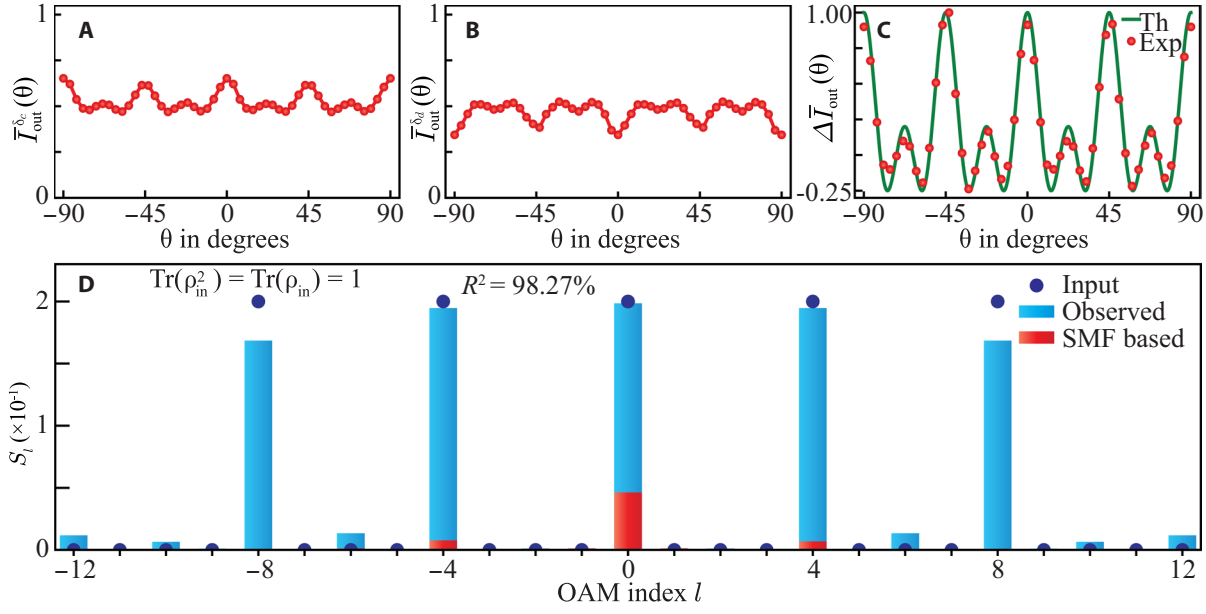

Fig. 4. Experimentally measured OAM probability distribution of discrete pure state. (**A** and **B**) Plots of the photon detection probability $\bar{I}^{\delta}_{out}(\theta)$ as a function of the rotation angle θ at $\delta = \delta_c \approx 0$ and $\delta = \delta_d \approx \pi$. (**C**) Experimentally measured polarization-corrected difference probability $\Delta I_{out}(\theta)$ as a function of θ. The red dots are the experiments, and the solid green line is the theory. (**D**) Reconstructed OAM spectrum. Blue bars are the measured spectrum, while the blue dots are the input spectrum; the red bars represent the performance of an SMF-based detector.

and observed spectra is much better. This can be observed through the results presented in Fig. 5D. In this case, since the input state was naturally produced using the nonlinear optical process of SPDC, there was no generation error and it could be very accurately predicted by the theory. As a consequence, the measurement accuracy for this dataset is higher. We further note that because of the issues related to generation accuracy, we only use data presented in Fig. 5D for estimating the detection efficiency presented in Fig. 6.

Analyzing the uniformity of detection efficiency

One of the objectives of this work is to develop a detector that has uniform detection efficiency over a broad range of OAM modes as

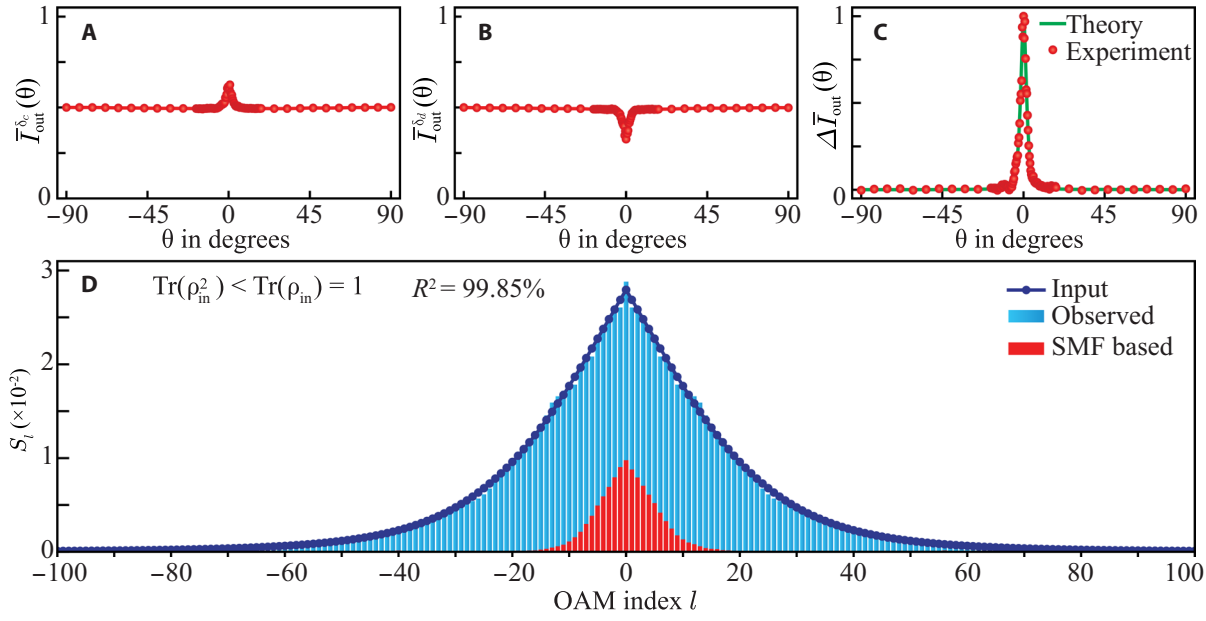

Fig. 5. OAM probability distribution of a single-photon diagonal mixed state produced by SPDC. (**A** and **B**) Plots of the photon detection probability $\bar{I}^{\delta}_{out}(\theta)$ as a function of the rotation angle θ at $\delta = \delta_c \approx 0$ and $\delta = \delta_d \approx \pi$. (**C**) Experimentally measured polarization-corrected difference probability $\Delta I_{out}(\theta)$ as a function of θ. The red dots are the experiments, and the solid green line is the theory. (**D**) Reconstructed OAM spectrum. Blue bars are the measured spectrum, while the blue dots are the input spectrum; the red bars represent the performance of an SMF-based detector.

opposed to the SMF-based detectors (*25*, *26*). We take the mode detection efficiency η_l of our scheme to be

$$\eta_l = \kappa \frac{S_l^{ob}}{S_l^{in}} \times 100 \tag{8}$$

where κ is the overall quantum efficiency of the detection system. S_l^{in} and S_l^{ob} are the input and the observed OAM spectra. Since the results reported in Fig. 5D have the lowest state generation error, we use these for estimating η_l and plot it in Fig. 6. The factor η_l / κ is uniform over $|l|$, demonstrating a broadband mode–independent detection efficiency. The increase in the variance of η_l / κ at large $|l|$ is attributed to decreasing signal-to-noise ratio of the dataset at large $|l|$, which eventually becomes unfit for estimating η_l beyond $|l| = 40$.

DISCUSSION

In conclusion, we have proposed and demonstrated a broadband, uniform-efficiency OAM-mode detector that measures the true OAM-mode spectrum, is noise insensitive, and is capable of measuring the OAM spectrum of an arbitrary quantum state without any previous information at both high-light and single-photon levels. Such an OAM-mode detector can have important consequences for OAM-based photonic quantum technologies, such as the high-dimensional cryptography protocols (*58*) and optical communications (*6*), quantum computing (*59*), quantum metrology (*60*, *61*), and quantum imaging (*62*, *63*). We believe that the OAM-mode detector reported here will not only render the existing OAM-based applications more viable but also enable novel OAM-based quantum technologies.

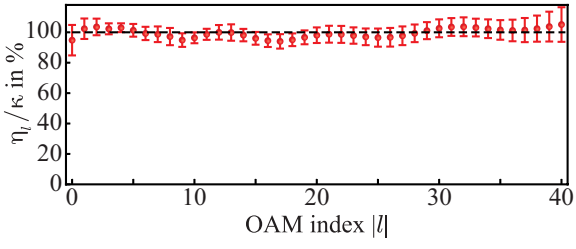

Fig. 6. Estimated detection efficiency as a function of $|l|$.

To emphasize the noise-insensitive aspect of our technique, we note that in panels (A) and (B) of Figs. 2 to 5, the plots of $\bar{I}^{\delta_c}_{out}(\theta)$ and $\bar{I}^{\delta_d}_{out}(\theta)$ contain large background contributions, resulting in poor contrast, the main sources of which are the EMCCD dark counts and the ambient light. This is because, in our experiment, the transverse size of the field falling onto the EMCCD is much smaller than the EMCCD sensor size. As a result, only a small fraction of the EMCCD pixels is involved in detecting the field and contributing to the signal; the remaining pixels only contribute to noise. Nonetheless, as shown in panel (C), the noise contributions $I_n^{\delta_c}(\theta)$ and $I_n^{\delta_d}(\theta)$ cancel each other in the difference probability $\Delta\bar{I}_{out}(\theta)$, which becomes almost free of such noise. As a result, our technique becomes extremely insensitive to noise sources and thus achieves very high detection fidelity even in the presence of substantial noise. This is in contrast to the most widely used method of OAM-mode detection based on an SLM and an SMF (*25*, *26*) that cannot filter out such noise sources and thus get adversely affected by them.

In addition to being noise insensitive, our technique does not involve loss of the input state and can be very fast. A careful alignment of our homebuilt IR brings the angular deviations to about 30 μ-radians, and we observed that a realignment of IR was required only if θ was changed by more than 30°. Therefore, if there is previous

information that the angular width of $\bar{I}^{\delta}_{\text{out}}(\theta)$ is less than 30°, then no realignment is required. However, if we have no previous information or if $\bar{I}^{\delta}_{\text{out}}(\theta)$ has larger angular widths, realignments are required. For the spectra reported in Figs. 2, 3, and 5, no realignment was required and the entire data taking was finished within a few minutes. However, for the spectra in Fig. 4, realignments were done, increasing the data taking time proportionately.

We note that our approach for broadband OAM-mode detection ensures unique features such as (i) uniform detection efficiency, (ii) true spectrum measurement without post-selecting on a particular radial mode, (iii) no need for previous information, and (iv) insensitivity to phase-uncorrelated background. However, our present implementation technique that has been demonstrated for the diagonal elements of an arbitrary density matrix in the OAM basis cannot be used for measuring the off-diagonal elements, which contains information about whether two given OAM modes are phase coherent or phase incoherent with respect to each other. Nonetheless, if such an approach could be extended to off-diagonal elements, then for an arbitrary density matrix even the off-diagonal elements could be measured with high fidelity and the measurement scheme by default would have all the unique features of this approach.

The prime reason for stringent alignment and stability requirements in our technique is the unavailability of IRs with near-zero angular deviations and faster rotation speeds. If such image rotators become commercially available, the alignment and stability requirements as well as the measurement time will reduce proportionately, making our technique suitable even for applications that require very fast measurements. Until such IRs become commercially available, the existing techniques such as those based on an SLM and an SMF may be preferred in situations in which the dimensionality of the state is very low and the true state measurement with high fidelity is not crucial. However, for any high-dimensional applications requiring accurate, noise-robust, and high-fidelity measurement of OAM spectrum, our technique would be most suited. Also, although our technique is not based on having previous knowledge of the input state, leveraging such knowledge, as is done in compressive sensing–based methods (*36*), can further reduce the alignment requirements and markedly increase the measurement speeds.

MATERIALS AND METHODS

Polarization calibration of the interferometer

To bypass the polarization issues caused by the rotation of the IR, the interferometer needs to be calibrated according to Eq. 3 by measuring both I_2^{tot} and $I_{2x}(\theta)$ and thus $\cos[\psi(\theta)]$. The probabilities I_2^{tot} and $I_{2x}(\theta)$ can be measured by blocking the upper arm of the interferometer. For measuring $I_{2x}(\theta)$, we place a polarizer along $\hat{\mathbf{x}}$, right before the EMCCD, and measure the probability as a function of θ. We note that I_2^{tot} is the total probability through the IR without any polarizer and thus that it is independent of θ. Figure 7 shows the plot of $\frac{1}{\cos[\psi(\theta)]} = \sqrt{\frac{I_2^{\text{tot}}}{I_{2x}(\theta)}}$ and is used for calculating $\Delta I_{\text{out}}(\theta)$ using Eq. 3 for the results reported in Figs. 2 to 5.

Details of the experimental setup in Fig. 1A

In this experimental setup, we generate high-dimensional OAM states using a He-Ne laser of wavelength 633 nm and a beam waist of 0.4 mm. We make the Gaussian beam go through a spatial filter and

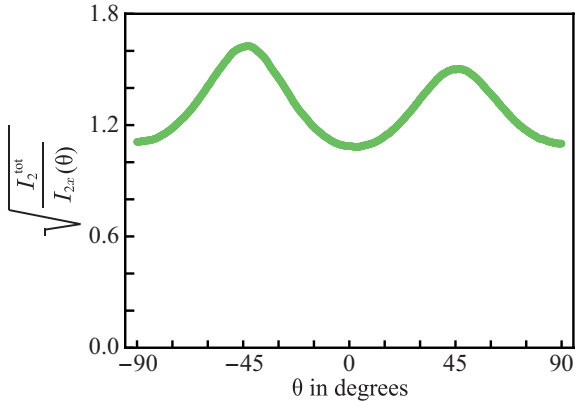

Fig. 7. Measured $\frac{1}{\cos[\psi(\theta)]} = \sqrt{\frac{I_2^{\text{tot}}}{I_{2x}(\theta)}}$ as a function of θ.

then magnify it using a 4f configuration with lenses of focal lengths 13.86 and 200 mm. The resulting beam is projected onto a Holoeye Pluto-2-NIR-011 SLM. We use the method by Arrizón *et al.* (*54*) to imprint a suitable hologram on the SLM for producing a desired coherent superposition of $\text{LG}^{|l|}_{p=0}$ modes. The generated state is obtained at the first diffraction order of the SLM. To measure the probability, we use an Andor iXon Ultra897 EMCCD camera with a 512 × 512 pixel grid and a pixel pitch of 16 × 16 μm^2. EMCCD gain is set at 1 with sufficient neutral density filter to avoid saturation.

Details of the experimental setup in Fig. 1B

In this setup, we generate single-photon states by producing SPDC photons in a type-I BBO crystal of thickness 15 mm, pumped by an ultraviolet (UV) 100-mW TOPTICA TopMode continuous wave laser of wavelength 405 nm with beam waist 388 μm. A dichroic filter is used for blocking the UV laser source while allowing the down-converted photons at 810 nm to pass through. Subsequently, the down-converted photons are filtered through a 10-nm bandwidth interference filter having a central wavelength of 810 nm. The crystal plane is imaged with a magnification of 6 using the 4f configuration with lenses of focal lengths 50 and 300 mm. The Fourier transform of this magnified image is obtained at the EMCCD plane using a lens of focal length 500 mm. The EMCCD is used with a gain of 300 and an acquisition time of 0.4 s.

We note that since we are using collinear down-conversion, the individual signal and idler photons have equal probability of arriving at the EMCCD. Therefore, the camera records the sum of photon count rates due to signal and idler fields. However, since the individual signal and idler fields have the same OAM spectrum, the difference probability $\Delta I_{\text{out}}(\theta)$ due to the signal and idler photons is also the same. Here, we have assumed that the probability of the simultaneous arrival of the signal and idler photons at the same EMCCD pixel is negligibly small. This assumption is justified given that the EMCCD has 512 × 512 pixels, and we work at the level of only a few photons per EMCCD frame.

Aligning the interferometer in Fig. 1C

In our experiment, first we align the IR manually to reduce the angular deviations of the field passing through it to be less than 1 milliradian. We then insert two mirrors M_1 and M_2 with actuator-based

control after the IR and use a feedback mechanism for automated alignment. To track the center of the Gaussian beam from the He-Ne laser at two locations, we use two cameras placed at the output ports of the beam splitter. One camera is a charge-coupled device (CCD) camera with a pixel grid of 2592×2048, while the other is the EMCCD camera. Next, we manually align the interferometer for zero fringe condition with a Gaussian beam and block the upper interferometric arm containing Q-H-Q to determine the coordinates of the center of the beam falling on each camera. These coordinates serve as the target coordinates for alignment at each subsequent θ, if re-alignment is required. We then center the beam by electronically adjusting the mirrors M_1 and M_2 through an iterative algorithm. For this, we make sure that the distance between the EMCCD and BS_2 is far greater than that between the CCD and BS_2. Then, by adjusting M_1, we bring the beam toward the CCD target center, and by adjusting M_2, we bring the beam toward the EMCCD target center. This way, we are able to align the fields to within 30.5 μ-radian to the EMCCD. To set the interferometer for $\delta = \delta_c$ and $\delta = \delta_d$ conditions, we remove the blocker from the upper arm and record the output intensity I at the EMCCD camera for a Gaussian input beam. We take five such intensity measurements at five different orientations β of the half-wave plate, separated by 36°. We fit these measurements with the function $I = a + b\cos 2(\beta - c)$ and obtain the orientation at which I is maximum and thus obtain $\delta \approx 0$. From this orientation, we rotate the half-wave plate by 90° to obtain the $\delta \approx \pi$ condition. We then measure the probabilities $\bar{I}^{\delta_c}_{\text{out}}(\theta)$ and $\bar{I}^{\delta_d}_{\text{out}}(\theta)$. To reduce the effects due to thermal and air-flow fluctuations, we cover the interferometer with a box and wait for it to stabilize.

Rotation resolution and OAM spectrum reconstruction

Our technique requires S_l to be reconstructed from the measured $\Delta I_{\text{out}}(\theta)$ through Fourier transformation. According to the Whittaker-Shannon sampling theorem (*64*), the sampling rate of a signal should be at least twice its highest frequency to completely characterize the signal. So, for our scheme, if the highest OAM index of the incident state is l_{max}, the step size for θ should be smaller than $180°/(2l_{\text{max}} + 1)$. Therefore, to reconstruct an OAM spectrum having l_{max} number of modes, one needs to measure $\Delta I_{\text{out}}(\theta)$ at a minimum of $2l_{\text{max}}$ number of θ points. Nonetheless, since we do not use any previous information about the input state including its dimensionality, we first measure $\Delta I_{\text{out}}(\theta)$ at fewer numbers of θ values to get some idea about the functional form of $\Delta I_{\text{out}}(\theta)$, and then repeat the measurements of $\Delta I_{\text{out}}(\theta)$ at an appropriate number of θ values as dictated by the sampling theorem. For the state reported in Figs. 2 to 4, we measure $\Delta I_{\text{out}}(\theta)$ at θ values separated by 3.6°. For the state reported in Figs. 3 and 5, the variation of $\Delta I_{\text{out}}(\theta)$ is maximum in the range $\theta = -18°$ to $\theta = 18°$. So, for this range, we take measurements at θ values separated by 0.36°, while for the remaining range, the separation is 7.2°.

Effects due to the angular deviation of the image rotator

In our technique, it is very important that the output intensity $\bar{I}^{\delta}_{\text{out}}(\theta)$ as a function of rotation angle θ is measured correctly. For this, it is necessary that the two fields interfering at the second beam splitter (BS_2) of Fig. 1C have perfect overlap; any deviation from the perfect overlap results in error in the measurement of $\bar{I}^{\delta}_{\text{out}}(\theta)$ and thus in the estimated spectrum. However, due to manufacturing errors, IRs invariably introduce angular deviations in the transmitted field, resulting in decreased overlap as a function of θ. In section S6, we present a detailed analysis of the effects due to angular deviation. In that section, through illustrative figures and numerical analysis, we show how angular deviation of an image rotator affects the measurement of $\bar{I}^{\delta}_{\text{out}}(\theta)$. We find that with a commercial Dove prism having angular deviation greater than 10000 μ-radians, the average fractional overlap of the two fields is less than 0.1, which implies a very inaccurate measurement of $\bar{I}^{\delta}_{\text{out}}(\theta)$. On the other hand, for the homebuilt image rotator reported here, having angular deviations less that 30 μ-radians, the average fractional overlap is close to 1, resulting in a very accurate measurement of $\bar{I}^{\delta}_{\text{out}}(\theta)$.

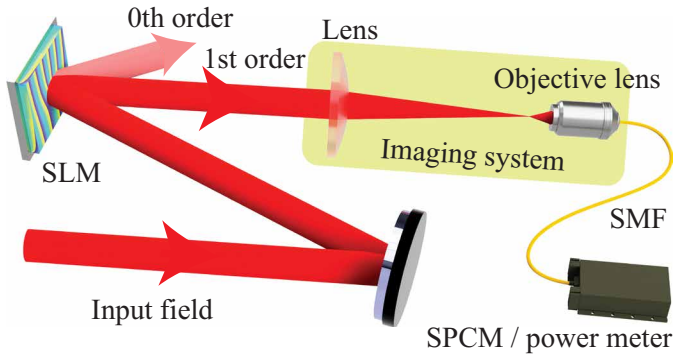

Fig. 8. Experimental setup for OAM-mode detection using an SLM and an SMF. SPCM, single-photon counting module.

Details of the experimental setup for SMF-based OAM measurement

Figure 8 shows the experimental setup for an SMF-based measurement (*25*, *26*). For the input spectra produced using the setup of Fig. 1 (A and B), we couple the first-order diffraction output from the SLM to the SMF by imaging the SLM plane onto the SMF using a 500-mm focal length lens and a Newport 60× objective with effective focal length 2.9 mm in a 4f configuration. In this configuration, we obtain $\sigma / w_0 = 0.6$, where $\sigma = M\sigma_{\text{smf}}$, w_0 is the beam waist of the OAM modes, σ_{smf} is the core radius of the SMF, and M is the magnification of the imaging system. The SMF is then coupled to a single-photon avalanche diode detector to measure the OAM spectrum. For the state generated using the setup of Fig. 1B, we image the BBO crystal of Fig. 1B onto the SLM.

Supplementary Materials

This PDF file includes:

Supplementary Sections S1 to S6
Figs. S1 to S5

REFERENCES AND NOTES

1. L. Allen, M. W. Beijersbergen, R. J. C. Spreeuw, J. P. Woerdman, Orbital angular momentum of light and the transformation of Laguerre-Gaussian laser modes. *Phys. Rev. A* **45**, 8185–8189 (1992).
2. A. E. Willner, H. Huang, Y. Yan, Y. Ren, N. Ahmed, G. Xie, C. Bao, L. Li, Y. Cao, Z. Zhao, J. Wang, M. P. J. Lavery, M. Tur, S. Ramachandran, A. F. Molisch, N. Ashrafi, S. Ashrafi, Optical communications using orbital angular momentum beams. *Adv. Opt. Photonics* **7**, 66 (2015).
3. M. Erhard, R. Fickler, M. Krenn, A. Zeilinger, Twisted photons: New quantum perspectives in high dimensions. *Light Sci. Appl.* **7**, 17146 (2018).

4. J. Wang, J.-Y. Yang, I. M. Fazal, N. Ahmed, Y. Yan, H. Huang, Y. Ren, Y. Yue, S. Dolinar, M. Tur, A. E. Willner, Terabit free-space data transmission employing orbital angular momentum multiplexing. *Nat. Photonics* **6**, 488–496 (2012).
5. Y. Yan, G. Xie, M. P. J. Lavery, H. Huang, N. Ahmed, C. Bao, Y. Ren, Y. Cao, L. Li, Z. Zhao, A. F. Molisch, M. Tur, M. J. Padgett, A. E. Willner, High-capacity millimetre-wave communications with orbital angular momentum multiplexing. *Nat. Commun.* **5**, 4876 (2014).
6. N. Bozinovic, Y. Yue, Y. Ren, M. Tur, P. Kristensen, H. Huang, A. E. Willner, S. Ramachandran, Terabit-scale orbital angular momentum mode division multiplexing in fibers. *Science* **340**, 1545–1548 (2013).
7. N. J. Cerf, M. Bourennane, A. Karlsson, N. Gisin, Security of quantum key distribution using d-level systems. *Phys. Rev. Lett.* **88**, 127902 (2002).
8. G. M. Nikolopoulos, K. S. Ranade, G. Alber, Error tolerance of two-basis quantum-key-distribution protocols using qudits and two-way classical communication. *Phys. Rev. A* **73**, 032325 (2006).
9. T. C. Ralph, K. J. Resch, A. Gilchrist, Efficient Toffoli gates using qudits. *Phys. Rev. A* **75**, 022313 (2007).
10. B. P. Lanyon, M. Barbieri, M. P. Almeida, T. Jennewein, T. C. Ralph, K. J. Resch, G. J. Pryde, J. L. O'Brien, A. Gilchrist, A. G. White, Simplifying quantum logic using higher-dimensional Hilbert spaces. *Nat. Phys.* **5**, 134–140 (2009).
11. V. D'Ambrosio, N. Spagnolo, L. Del Re, S. Slussarenko, Y. Li, L. C. Kwek, L. Marrucci, S. P. Walborn, L. Aolita, F. Sciarrino, Photonic polarization gears for ultra-sensitive angular measurements. *Nat. Commun.* **4**, 2432 (2013).
12. A. K. Jha, G. S. Agarwal, R. W. Boyd, Supersensitive measurement of angular displacements using entangled photons. *Phys. Rev. A* **83**, 053829 (2011).
13. D. Kaszlikowski, P. Gnaciński, M. Żukowski, W. Miklaszewski, A. Zeilinger, Violations of local realism by two entangled N-dimensional systems are stronger than for two qubits. *Phys. Rev. Lett.* **85**, 4418–4421 (2000).
14. D. Collins, N. Gisin, N. Linden, S. Massar, S. Popescu, Bell inequalities for arbitrarily high-dimensional systems. *Phys. Rev. Lett.* **88**, 040404 (2002).
15. T. Vértesi, S. Pironio, N. Brunner, Closing the detection loophole in Bell experiments using qudits. *Phys. Rev. Lett.* **104**, 060401 (2010).
16. A. C. Dada, J. Leach, G. S. Buller, M. J. Padgett, E. Andersson, Experimental high-dimensional two-photon entanglement and violations of generalized Bell inequalities. *Nat. Phys.* **7**, 677–680 (2011).
17. V. D'Ambrosio, E. Nagali, S. P. Walborn, L. Aolita, S. Slussarenko, L. Marrucci, F. Sciarrino, Complete experimental toolbox for alignment-free quantum communication. *Nat. Commun.* **3**, 961 (2012).
18. G. Vallone, V. D'Ambrosio, A. Sponselli, S. Slussarenko, L. Marrucci, F. Sciarrino, P. Villoresi, Free-space quantum key distribution by rotation-invariant twisted photons. *Phys. Rev. Lett.* **113**, 060503 (2014).
19. A. Bhattacharjee, M. K. Joshi, S. Karan, J. Leach, A. K. Jha, Propagation-induced revival of entanglement in the angle-OAM bases. *Sci. Adv.* **8**, eabn7876 (2022).
20. A. Sit, F. Bouchard, R. Fickler, J. Gagnon-Bischoff, H. Larocque, K. Heshami, D. Elser, C. Peuntinger, K. Günthner, B. Heim, C. Marquardt, G. Leuchs, R. W. Boyd, E. Karimi, High-dimensional intracity quantum cryptography with structured photons. *Optica* **4**, 1006–1010 (2017).
21. F. Bouchard, A. Sit, F. Hufnagel, A. Abbas, Y. Zhang, K. Heshami, R. Fickler, C. Marquardt, G. Leuchs, E. Karimi, R. W. Boyd, Quantum cryptography with twisted photons through an outdoor underwater channel. *Opt. Express* **26**, 22563–22573 (2018).
22. F. Brandt, M. Hiekkamäki, F. Bouchard, M. Huber, R. Fickler, High-dimensional quantum gates using full-field spatial modes of photons. *Optica* **7**, 98–107 (2020).
23. X.-M. Hu, W.-B. Xing, B.-H. Liu, D.-Y. He, H. Cao, Y. Guo, C. Zhang, H. Zhang, Y.-F. Huang, C.-F. Li, G.-C. Guo, Efficient distribution of high-dimensional entanglement through 11 km fiber. *Optica* **7**, 738–743 (2020).
24. Z. Ma, P. Kristensen, S. Ramachandran, Scaling information pathways in optical fibers by topological confinement. *Science* **380**, 278–282 (2023).
25. A. Mair, A. Vaziri, G. Weihs, A. Zeilinger, Entanglement of the orbital angular momentum states of photons. *Nature* **412**, 313–316 (2001).
26. N. R. Heckenberg, R. McDuff, C. P. Smith, A. G. White, Generation of optical phase singularities by computer-generated holograms. *Opt. Lett.* **17**, 221–223 (1992).
27. H. Di Lorenzo Pires, J. Woudenberg, M. P. van Exter, Measurement of the orbital angular momentum spectrum of partially coherent beams. *Opt. Lett.* **35**, 889–891 (2010).
28. H. Di Lorenzo Pires, H. C. B. Florijn, M. P. van Exter, Measurement of the spiral spectrum of entangled two-photon states. *Phys. Rev. Lett.* **104**, 020505 (2010).
29. M. Malik, S. Murugkar, J. Leach, R. W. Boyd, Measurement of the orbital-angular-momentum spectrum of fields with partial angular coherence using double-angular-slit interference. *Phys. Rev. A* **86**, 063806 (2012).
30. M. V. Vasnetsov, J. P. Torres, D. V. Petrov, L. Torner, Observation of the orbital angular momentum spectrum of a light beam. *Opt. Lett.* **28**, 2285 (2003).
31. H.-L. Zhou, D.-Z. Fu, J.-J. Dong, P. Zhang, D.-X. Chen, X.-L. Cai, F.-L. Li, X.-L. Zhang, Orbital angular momentum complex spectrum analyzer for vortex light based on the rotational Doppler effect. *Light Sci. Appl.* **6**, e16251 (2017).
32. J. Leach, M. J. Padgett, S. M. Barnett, S. Franke-Arnold, J. Courtial, Measuring the orbital angular momentum of a single photon. *Phys. Rev. Lett.* **88**, 257901 (2002).
33. H. Qassim, F. M. Miatto, J. P. Torres, M. J. Padgett, E. Karimi, R. W. Boyd, Limitations to the determination of a Laguerre–Gauss spectrum via projective, phase-flattening measurement. *J. Opt. Soc. Am. B* **31**, A20–A23 (2014).
34. J. P. Torres, A. Alexandrescu, L. Torner, Quantum spiral bandwidth of entangled two-photon states. *Phys. Rev. A* **68**, 050301 (2003).
35. G. Kulkarni, R. Sahu, O. S. Magaña-Loaiza, R. W. Boyd, A. K. Jha, Single-shot measurement of the orbital-angular-momentum spectrum of light. *Nat. Commun.* **8**, 1054 (2017).
36. F. Tonolini, S. Chan, M. Agnew, A. Lindsay, J. Leach, Reconstructing high-dimensional two-photon entangled states via compressive sensing. *Sci. Rep.* **4**, 6542 (2014).
37. F. Bouchard, N. H. Valencia, F. Brandt, R. Fickler, M. Huber, M. Malik, Measuring azimuthal and radial modes of photons. *Opt. Express* **26**, 31925–31941 (2018).
38. M. Hiekkamäki, S. Prabhakar, R. Fickler, Near-perfect measuring of full-field transverse-spatial modes of light. *Opt. Express* **27**, 31456–31464 (2019).
39. D. I. Shahar, H. B. Kabagöz, S. Ramachandran, Generation of spatial combs digitized by orbital angular momentum. *APL Photonics* **9**, 016113 (2024).
40. S. Choudhary, R. Sampson, Y. Miyamoto, O. S. Magaña-Loaiza, S. M. H. Rafsanjani, M. Mirhosseini, R. W. Boyd, Measurement of the radial mode spectrum of photons through a phase-retrieval method. *Opt. Lett.* **43**, 6101–6104 (2018).
41. A. K. Jha, J. Leach, B. Jack, S. Franke-Arnold, S. M. Barnett, R. W. Boyd, M. J. Padgett, Angular two-photon interference and angular two-qubit states. *Phys. Rev. Lett.* **104**, 010501 (2010).
42. M. Malik, M. Mirhosseini, M. P. J. Lavery, J. Leach, M. J. Padgett, R. W. Boyd, Direct measurement of a 27-dimensional orbital-angular-momentum state vector. *Nat. Commun.* **5**, 3115 (2014).
43. J. S. Lundeen, C. Bamber, Procedure for direct measurement of general quantum states using weak measurement. *Phys. Rev. Lett.* **108**, 070402 (2012).
44. Y. Zhou, J. Zhao, D. Hay, K. McGonagle, R. W. Boyd, Z. Shi, Direct tomography of high-dimensional density matrices for general quantum states of photons. *Phys. Rev. Lett.* **127**, 040402 (2021).
45. G. Kulkarni, S. Karan, A. K. Jha, Measurement of pure states of light in the orbital-angular-momentum basis using nine multipixel image acquisitions. *Phys. Rev. Appl.* **13**, 054077 (2020).
46. G. Kulkarni, L. Taneja, S. Aarav, A. K. Jha, Angular Schmidt spectrum of entangled photons: Derivation of an exact formula and experimental characterization for noncollinear phase matching. *Phys. Rev. A* **97**, 063846 (2018).
47. M. Mirhosseini, O. S. Magaña-Loaiza, C. Chen, S. M. Hashemi Rafsanjani, R. W. Boyd, Wigner distribution of twisted photons. *Phys. Rev. Lett.* **116**, 130402 (2016).
48. M. Mirhosseini, M. Malik, Z. Shi, R. W. Boyd, Efficient separation of the orbital angular momentum eigenstates of light. *Nat. Commun.* **4**, 2781 (2013).
49. M. P. J. Lavery, D. J. Robertson, G. C. G. Berkhout, G. D. Love, M. J. Padgett, J. Courtial, Refractive elements for the measurement of the orbital angular momentum of a single photon. *Opt. Express* **20**, 2110–2115 (2012).
50. G. C. G. Berkhout, M. P. J. Lavery, J. Courtial, M. W. Beijersbergen, M. J. Padgett, Efficient sorting of orbital angular momentum states of light. *Phys. Rev. Lett.* **105**, 153601 (2010).
51. N. K. Fontaine, R. Ryf, H. Chen, D. T. Neilson, K. Kim, J. Carpenter, Laguerre-Gaussian mode sorter. *Nat. Commun.* **10**, 1865 (2019).
52. R. Sahu, S. Chaudhary, K. Khare, M. Bhattacharya, H. Wanare, A. K. Jha, Angular lens. *Opt. Express* **26**, 8709 (2018).
53. S. Karan, R. , P. Mohta, A. K. Jha, Quantifying polarization changes induced by rotating dove prisms and k-mirrors. *Appl. Opt.* **61**, 8302–8307 (2022).
54. V. Arrizón, U. Ruiz, R. Carrada, L. A. González, Pixelated phase computer holograms for the accurate encoding of scalar complex fields. *J. Opt. Soc. Am. A* **24**, 3500–3507 (2007).
55. L. Mandel, E. Wolf, *Optical Coherence and Quantum Optics* (Cambridge Univ. Press, 1995).
56. A. Bhattacharjee, R. Sahu, A. K. Jha, Generation of a gaussian schell-model field as a mixture of its coherent modes. *J. Opt.* **21**, 105601 (2019).
57. S. Karan, S. Aarav, H. Bharadhwaj, L. Taneja, A. De, G. Kulkarni, N. Meher, A. K. Jha, Phase matching in β-barium borate crystals for spontaneous parametric down-conversion. *J. Opt.* **22**, 083501 (2020).
58. M. Mirhosseini, O. S. Magaña-Loaiza, M. N. O'Sullivan, B. Rodenburg, M. Malik, M. P. J. Lavery, M. J. Padgett, D. J. Gauthier, R. W. Boyd, High-dimensional quantum cryptography with twisted light. *New J. Phys.* **17**, 033033 (2015).
59. A. Babazadeh, M. Erhard, F. Wang, M. Malik, R. Nouroozi, M. Krenn, A. Zeilinger, High-dimensional single-photon quantum gates: Concepts and experiments. *Phys. Rev. Lett.* **119**, 180510 (2017).
60. M. P. J. Lavery, F. C. Speirits, S. M. Barnett, M. J. Padgett, Detection of a spinning object using light's orbital angular momentum. *Science* **341**, 537–540 (2013).
61. N. Cvijetic, G. Milione, E. Ip, T. Wang, Detecting lateral motion using light's orbital angular momentum. *Sci. Rep.* **5**, 15422 (2015).
62. L. Chen, J. Lei, J. Romero, Quantum digital spiral imaging. *Light Sci. Appl.* **3**, –e153 (2014).
63. L. Torner, J. P. Torres, S. Carrasco, Digital spiral imaging. *Opt. Express.* **13**, 873–881 (2005).

64. J. W. Goodman, *Introduction to Fourier Optics* (Roberts and Company Publishers, 2005).

Acknowledgments: We thank S. Wanare and S. Pandey for their initial contributions in implementing the image rotator. **Funding:** We acknowledge financial support from the Science and Engineering Research Board through grants STR/2021/000035 and CRG/2022/003070 and from the Department of Science & Technology, Government of India through grant DST/ICPS/QuST/Theme-1/2019). S.K. thanks the University Grant Commission (UGC), Government of India for financial support. **Author contributions:** A.K.J. and S.K. proposed and developed the idea. S.K. performed the experiments with help from A.K.J. M.P.V.E. provided the high-quality homebuilt IR. A.K.J. and S.K. wrote the manuscript with inputs from M.P.V.E. A.K.J. supervised the overall work. **Competing interests:** S.K. and A.K.J. are authors on a patent related to this work filed by Indian Institute of Technology Kanpur (no. 202411014104, filed 27 February 2024, published 8 March 2024). The authors declare no other competing interests. **Data and materials availability:** All data needed to evaluate the conclusions in the paper are present in the paper and/or the Supplementary Materials.

Submitted 29 May 2024
Accepted 7 February 2025
Published 14 March 2025
10.1126/sciadv.adq7201